Effect of Power-Law Parameters on Time Step Size in CFD-DEM Simulations of Non-newtonian Fluid-Driven Fracture

Daniyar Kazidenov and Yerlan Amanbek(✉)

Department of Mathematics, School of Sciences and Humanities, Nazarbayev University, Kabanbay Batyr 53, Astana, Kazakhstan
{daniyar.kazidenov,yerlan.amanbek}@nu.edu.kz

Abstract. Selection of a suitable time step size is essential for accurate CFD-DEM simulations involving non-Newtonian fluids. This study explores the effect of power-law parameters, the consistency index (K) and the flow behavior index (n), on time step sensitivity during fluid-driven fracture initiation in granular media. The results show that the power-law parameters have a strong effect on fracturing behavior. Less viscous fluids create infiltration-dominated linear fractures with lower peak pressures, while more viscous fluids produce wider fractures dominated by grain displacement and higher peak pressures. The analysis of injection pressures at various time step sizes indicates that CFD time step sensitivity is influenced more by the flow behavior index rather than the consistency index. Lower flow behavior indices ($n = 0.1$ and 0.2) demonstrate relatively accurate results at a higher time step ($\Delta t = 10^{-4}$s). In contrast, when n increases to 0.3, the errors become more significant, which in turn requires a reduction in the time step to $\Delta t = 10^{-5}$s.

Keywords: Time step · Fracture initiation · CFD-DEM modeling

1 Introduction

Injection of polymer solutions underground, which is common practice in many subsurface applications, may result in the formation of fractures when the injecting fluid pressure exceeds the mechanical strength of the rock. The behavior and physical characteristics of these fractures are complicated and influenced by various factors, such as solid material properties, rock heterogeneity, in situ stress conditions, fluid rheology, and flow conditions [8,17,23]. Understanding the mechanisms of fracture initiation is crucial for predicting further fracture behavior and enhancing engineering design strategies for effective fracture management. Therefore, reliable and high-fidelity simulations are essential to accurately capture fluid flow dynamics and fluid-particle interactions, particularly when accounting for the non-Newtonian behavior of polymer solutions.

Numerical models based on the discrete element method (DEM) are commonly used to study fracture initiation and propagation. In DEM, the reservoir rock is represented as a granular medium consisting of individual particles. The material properties and interactions of particles can be defined according to the rock type. Modeling of

© The Author(s), under exclusive license to Springer Nature Switzerland AG 2026
O. Gervasi et al. (Eds.): ICCSA 2025 Workshops, LNCS 15888, pp. 433–446, 2026.
https://doi.org/10.1007/978-3-031-97596-7_29

fluid flow through porous regions between particles is performed by coupling DEM with other numerical approaches. In DEM-based simulations, fluid-driven fracturing occurs through particle displacements induced by fluid forces. Most studies examine mechanisms of fracture initiation by analyzing how fluid properties and flow conditions influence particle displacements. Particle displacement becomes the primary process instead of infiltration during the injection of more viscous fluids, contributing to fracture creation [25,26]. Similarly, an increase in injection rates results in larger fracture openings, reducing the fluid velocity and limiting the infiltration into the surrounding medium [10]. Numerous studies indicate that the fracturing process is strongly affected by solid material properties [22,25] and stress conditions [25].

The coupling of DEM with computational fluid dynamics (CFD) has been widely accepted as a reliable approach for simulating fluid-driven fracture initiation and propagation [20,21,24]. CFD-DEM is an Eulerian-Lagrangian approach that couples the fluid phase (Eulerian) with discrete particle interactions (Lagrangian). In CFD-DEM, fluid flow is represented as a continuous phase, and governed by the system of locally averaged Navier-Stokes equations for mass and momentum conservation, whereas particles are tracked individually and their motion is solved using Newton's second law. Particle-particle and particle-wall interactions are handled using contact models. The coupling of CFD and DEM integrates fluid-particle interactions, which are governed by drag force models. The coupling system is typically categorized into three groups based on fluid cell and particle sizes: unresolved, semi-resolved, and resolved. The unresolved setting uses larger fluid cells than the average particle size, whereas in the resolved approach, a particle is resolved by many small fluid cells. In the semi-resolved case, the particle size is approximately the same as the fluid cell size. The accuracy of coupling simulations is determined by the time step size and the coupling interval between CFD and DEM. Small time step sizes and intervals lead to more accurate results but with longer simulation time, while larger ones reduce simulation time with greater errors.

This study extends the findings of earlier research on fracture initiation induced by polymer solutions in granular media [13]. Injected polymer solutions demonstrate non-Newtonian behavior, which is represented by the power-law model. In this model, the fluid viscosity is characterized by two parameters: the consistency index (K) and the flow behavior index (n). These parameters directly influence the fluid's resistance to flow and, consequently, the injection pressure during fracturing. The accuracy of the pressure field is strongly influenced by both the selected time step size and the rheological parameters of the fluid. Therefore, selecting an appropriate time step size based on the specific rheological parameters is essential for maintaining simulation accuracy and stability. In this study, we numerically explore how the power law parameters affect time step size in the fluid phase of the fracture initiation model. Our primary aim is to optimize the time step size based on different combinations of these parameters.

2 Model Formulation

2.1 Governing Equations for the Solid Phase

In the current study, the fracture initiation process is modeled using the CFD-DEM coupling approach. DEM represents the rock as a granular medium consisting of individual particles, whereas CFD describes the fluid flow within the porous region of the medium. The interaction of the fluid phase with the solid phase is described by a fluid-particle interaction force.

The motion of particles is calculated by Newton's second law, which accounts for particle-particle and fluid-particle interactions, and gravity:

$$m_i \frac{d\boldsymbol{v}_i}{dt} = \boldsymbol{f}_{pf,i} + \sum_{j=1}^{k_c} \left(\boldsymbol{f}_{c,ij} + \boldsymbol{f}_{damp,ij}\right) + m_i \boldsymbol{g} \tag{1}$$

$$I_i \frac{d\boldsymbol{\omega}_i}{dt} = \sum_{j=1}^{k_c} \boldsymbol{T}_{ij} \tag{2}$$

where $\boldsymbol{v}_i$ and $\boldsymbol{\omega}_i$ represent the particle translational and angular velocities, m_i and I_i are the particle mass and inertia, $\boldsymbol{f}_{pf,i}$ is the sum of all forces acting by fluid on a particle, $\boldsymbol{f}_{c,ij}$, $\boldsymbol{f}_{damp,ij}$ and $\boldsymbol{T}_{ij}$ denote particle-particle contact force, viscous damping force and torque, $m_i\boldsymbol{g}$ is the gravitational force, and k_c is the number of contacting particles.

The particle-particle contact force is calculated using the modified version of the Johnson-Kendall-Roberts (JKR) contact model [11], where the surface energy density describes the cohesion (bonding) of particles. When the applied stress is greater than the adhesive strength, the particles unbond each other and no new bonds form after unbonding [12,14,16]. It is expressed in terms of the normal component of contact force:

$$\boldsymbol{f}_{c,ij}^{(n)} = \frac{4E^* a^3}{3R^*} - \sqrt{16\pi\gamma E^* a^3} \tag{3}$$

where $E^* = \left(\frac{1-\nu_1^2}{E_1} + \frac{1-\nu_2^2}{E_2}\right)^{-1}$ is the effective Young's modulus, where E_1, E_2 and ν_1, ν_2 represent the Young's modulus and the Poisson's ratio of the particles, γ denotes the surface energy density, a represents the radius of contacting surface, and $R^* = \left(\frac{R_i R_j}{R_i + R_j}\right)$ is the effective radius, where R_i and R_j represent the radius of particles.

In the fluid-particle interaction system, particles experience an additional force due to the surrounding fluid. The fluid-particle interaction force $\boldsymbol{f}_{pf,i}$ represents the sum of all forces exerted by the fluid on a particle:

$$\boldsymbol{f}_{pf,i} = \boldsymbol{f}_{d,i} + \boldsymbol{f}_{\nabla p,i} + \boldsymbol{f}_{\nabla\cdot\boldsymbol{\tau},i} + \boldsymbol{f}_{Ar,i} \tag{4}$$

where $\boldsymbol{f}_{d,i}$, $\boldsymbol{f}_{\nabla p,i}$, $\boldsymbol{f}_{\nabla\cdot\boldsymbol{\tau},i}$ and $\boldsymbol{f}_{Ar,i}$ denote the drag, pressure gradient, viscous and Archimedes forces, respectively.

2.2 Coupled CFD-DEM Model

The fluid flow in the porous region (α_f) of a granular medium is modeled by solving the Navier-Stokes equations with local averaging [28], where the pressure gradient, viscous and gravitational forces are merely shared between the fluid and solid phases:

$$\begin{cases} \frac{\partial \alpha_f}{\partial t} + \nabla \cdot (\alpha_f \boldsymbol{u}) = 0 \\ \frac{\partial (\rho_f \alpha_f \boldsymbol{u})}{\partial t} + \nabla \cdot \left(\rho_f \alpha_f \boldsymbol{u}\boldsymbol{u}\right) = -\alpha_f \nabla p + \alpha_f \nabla \cdot \boldsymbol{\tau} + \rho_f \alpha_f \boldsymbol{g} + \boldsymbol{F}_{pf}^{A} \end{cases} \tag{5}$$

where ρ_f, $\boldsymbol{u}$ and p denote the fluid's density, velocity and pressure, respectively, α_f is the volume fraction occupied by fluid in a granular medium, $\boldsymbol{\tau} = \mu_f \left((\nabla \boldsymbol{u}) + (\nabla \boldsymbol{u})^T\right)$ represents the stress tensor, where μ_f is the fluid dynamic viscosity and $\boldsymbol{F}_{pf}^{A} = \frac{1}{\Delta V} \sum_{i=1}^{n} \left(\boldsymbol{f}_{d,i} + \boldsymbol{f}_i^{''}\right)$ corresponds to the volumetric fluid-particle interaction force, where $\boldsymbol{f}_i^{''}$ includes all forces except drag, pressure gradient, and viscous forces, ΔV represents the fluid cell's volume.

The injected fluid is characterized as non-Newtonian and its rheology is described by the power-law model, expressing the viscosity as follows:

$$\mu_f(\dot{\gamma}) = K \dot{\gamma}^{(n-1)} \tag{6}$$

where $\dot{\gamma}$ represents the shear rate and K represents the consistency index, which describes the fluid's resistance to flow. Smaller values correspond to lower viscosity, whereas larger values indicate higher viscosity. n is the flow behavior index, which shows whether fluid is shear-thinning ($n < 1$), shear-thickening ($n > 1$), or Newtonian ($n = 1$).

The drag force is the dominant component in the overall fluid-particle interaction force, which directly influences particle motion and has an indirect effect on fluid dynamics. In the current study, the drag force model is derived from the modified Blake-Kozeny equation for the pressure drop [2] and corresponds to power-law fluid flow in multi-particle systems, accounting for the fluid's rheological parameters. This model includes power-law parameters (K and n), allowing a realistic representation of fluid rheology effect on drag force.

The drag force exerted on an individual particle is defined by:

$$\boldsymbol{f}_{d,i} = f \cdot \frac{\rho_f |\boldsymbol{u_i} - \boldsymbol{v_i}| (\boldsymbol{u_i} - \boldsymbol{v_i}) (1 - \alpha_f) V_{p,i}}{d_{p,i} \alpha_f} \tag{7}$$

where $f = \frac{\frac{150}{12} \left(9 + \frac{3}{n}\right)^n \alpha_f^{2(1-n)} (1 - \alpha_f)^n}{Re_{p,i}}$ denotes the Fanning friction factor, $\boldsymbol{u_i} - \boldsymbol{v_i}$ is the relative velocity between fluid and particle, $V_{p,i}$ and $d_{p,i}$ represent the particle volume and diameter, respectively and $Re_{p,i} = \frac{\rho_f d_{p,i}^n |\boldsymbol{u_i} - \boldsymbol{v_i}|^{2-n}}{K}$ is a particle Reynolds number, which incorporates power-law parameters of the fluid.

2.3 Calculation of Critical Simulation Time Step

The system of Navier-Stokes equations (Eq. 5) is numerically solved using the cfdemSolverPiso solver [18] based on Pressure-Implicit with Splitting of Operators (PISO) algorithm [9]. This approach uses the finite volume method (FVM) incorporating the momentum transfer between fluid and solid phases. In CFD-DEM coupling, the selection of appropriate time step is critical for achieving convergence in nonlinear calculations. A smaller time step results in more accurate results but increases simulation time, while a larger time step may cause instability and unrealistic behavior. In DEM, the critical time step is commonly calculated using methodologies based on material parameters such as mass and stiffness [1] and the Rayleigh time step [19]. The latter uses particle material parameters such as radius, density, shear modulus and Poisson's ratio. In CFD, the critical time step is typically computed using the Courant-Friedrichs-Lewy (CFL) condition [4] expressed as follows:

$$C = \Delta t \left(\sum_{i=1}^{n} \frac{u_i}{\Delta x_{cfd,i}} \right) \leq C_{max} \tag{8}$$

where C denotes the Courant number, Δt is the CFD time step, $\Delta x_{cfd,i}$ represents the size of a single cell and n indicates the number of spacial coordinates, which is typically $n = 1, 2$ and 3. Depending on the time-integration scheme of the solver, in general, C_{max} should have a value equal to or less than 1. Physically, the CFL condition requires that the flow should not propagate beyond a single cell in one time step.

In fluid flows dominated with diffusion and with lower Reynolds number, where viscous effects are significant, the critical time step is determined by diffusive time step criterion expressed as follows:

$$\Delta t \leq \frac{\Delta x_{cfd,i}^2}{2\nu} \tag{9}$$

where ν is the kinematic viscosity. From a physics standpoint, this criterion indicates that smaller cell sizes and high viscous fluids require smaller time steps. This typically important with explicit solvers where the time step has a greater influence on stability. However, in implicit solvers such as PISO, the time step can be larger, but accuracy and convergence should still be taken into account. In CFD-DEM coupling with PISO-based solvers, the CFD time step is much larger than DEM time step and should be selected carefully to achieve both stability and computational efficiency. In general, the coupling interval, which is the ratio between the CFD time step and the DEM time step, typically ranges between 10 and 100 in CFD-DEM simulations [15]. However, in creeping flows with lower Reynolds numbers, the coupling interval may vary.

3 Simulation Settings

In the current study, the numerical model replicates the Hele-Shaw cell experiment by injecting fluid into a sample confined under stress. In order to reduce computation cost, the half region and one layer of particles are used. The numerical model used in

this work has been successfully validated by comparing numerical results with experimental data of fracture initiation induced by power-law polymer solutions [13]. The schematic representation is shown in Fig. 1. The model includes solid phase and fluid phase domains of equal dimensions. The solid phase domain contains a total of 45000 particles of uniform size accommodated in a single layer. The dimensions of the region are 600 mm $\times$ 300 mm $\times$ 2 mm. A stress σ_3 is applied at the left and right boundaries, while $\sigma_1 = 2 \cdot \sigma_3$ is applied at the top boundary, and the bottom boundary is fixed. The interaction between the particles and walls is treated as frictionless.

The fluid phase domain consists of a total 10000 mesh cell configured as $50 \times 100 \times 2$ in the XYZ directions. The injection of fluid occurs through the inlet patch with size of 50 mm. Outlet patches are placed at the left, right and top boundaries. The boundary conditions are detailed in Table 1.

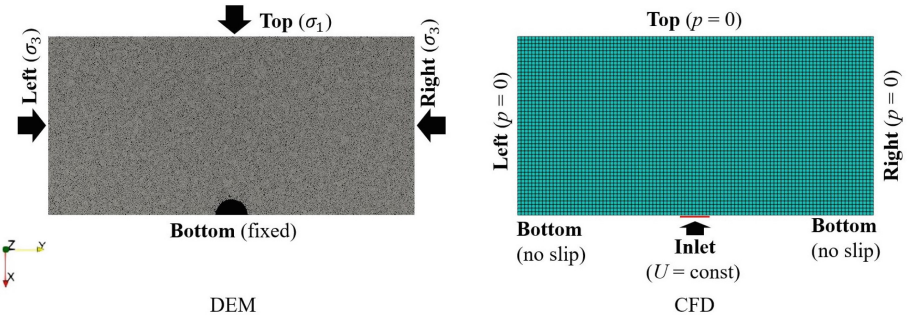

Fig. 1. Simulation setup for the fracture initiation model.

Table 1. Boundary conditions applied in fracture initiation simulations.

Boundary	DEM	CFD
Bottom	fixed	no slip
Inlet	fixed	$U = \text{const}$
Left	$\sigma_3 = \text{const}$	$p = 0$
Right	$\sigma_3 = \text{const}$	$p = 0$
Top	$\sigma_1 = \text{const}$	$p = 0$

Table 2 presents the material properties of the simulated particles. Most parameters including density, Poisson's ratio, Young's modulus and friction coefficient are primarily based on similar studies [21,24]. As the granular medium is assumed weakly cohesive, the surface energy density (γ) is set to a lower value of 1 J/m^2 ensuring weak bonding of particles.

Table 2. Particle material parameters used in the simulation.

Young's modulus, E (Pa)	10^6
Friction coefficient, μ	0.5
Density, ρ_p (kg/m^3)	2650
Poisson's ratio, ν	0.3
Surface energy density, γ (J/m^2)	1

The fluid cell size is chosen to meet the unresolved condition in CFD-DEM coupling, ensuring that each cell contains multiple particles [3]. The DEM time step is set to 10^{-5} s, which is equivalent to 3.48% of the critical time step based on the Rayleigh approach [19]. The CFD time step is defined as 10^{-4} and 10^{-5} s, maintaining a coupling interval of $N = 1$ and $N = 10$ for the current CFD-DEM framework. An open-source software package, CFDEM [6], is used for the simulations, which integrates the commercial DEM software Aspherix [18] and the open-source CFD software OpenFOAM [27]. A PISO-based algorithm is utilized to calculate the system of Navier-Stokes equations [7]. The first-order Euler scheme is used for time discretization, while the second-order Gauss linear scheme is applied for spatial derivatives. The simulation domain is decomposed into a $2 \times 4 \times 1$ grid configuration along the X, Y, and Z axes, respectively, for parallel processing across 8 cores.

The computational domain used in the current study is designed in three dimensions, but consists of only one solid particle layer and two fluid cells in the z-direction, effectively representing a quasi-2D configuration. This approach is selected to balance computational efficiency with the inherent three-dimensional requirements of the solvers used in the CFD-DEM framework. Due to the limited thickness of the domain, particle and fluid motions, as well as their interactions in the z-direction are negligible, thus corresponding to two-dimensional assumptions. Despite its simplicity, the current model is capable of capturing basic mechanisms of fluid-driven fracture initiation in granular media. Future work will focus on the use of fully three-dimensional configurations to investigate more complex fracture dynamics and extend their applicability to real-world applications.

4 Numerical Results

4.1 Effect of the Power-Law Parameters on Fracture Initiation

This study focuses on the injection of shear-thinning fluids ($n < 1$), as it represent the typical rheological properties of polymer solutions widely used in various subsurface applications such as enhanced oil recovery, hydraulic fracturing, and soil remediation. Many polymer-based solutions, such as partially hydrolyzed polyacrylamide (HPAM), xanthan gum, and guar gum, exhibit shear-thinning behavior, in which viscosity decreases with increasing shear rate. Accordingly, this section examines the effect of variations in rheological parameters on fracture initiation induced by different shear-thinning fluids. Table 3 presents the properties of injected fluids, including power-law

parameters. As presented in the table, all fluids have the same density and different consistency indices (K) ranging from 1 to 5 Pa·s. Each fluid is characterized by various flow behavior indices of 0.1, 0.2 and 0.3. The injection velocity in all simulation cases is $1.4 \cdot 10^{-3}$ m/s, corresponding to the creeping flow regime. The average particle Reynolds number is approximately $Re_p \approx 10^{-6}$.

Table 3. Injected fluid properties.

Fluid	Consistency index, K (Pa· s^n)	Flow behavior index, n	Density, ρ_f (kg/m^3)
Fluid A	1	0.1, 0.2, 0.3	998
Fluid B	2		
Fluid C	3		
Fluid D	4		
Fluid E	5		

Figure 2 demonstrates the snapshots of fracture initiation induced by power-law fluids with different rheological parameters (K and n). At $K = 1$ Pa·s, $n = 0.1$ (Fluid A), the fluid has less viscosity, which does not lead to any fractures. The fluid with $K = 2$ Pa·s, $n = 0.1$ (Fluid B) represents medium viscosity and creates a single linear fracture path perpendicular to the direction of less confining stress. $K = 5$ Pa·s, $n = 0.1$ (Fluid E) has more viscous behavior and creates wider radial fractures dominated by grain displacement. An increase in n from 0.2 to 0.3 enhances the effect of K and leads to a rise in overall viscosity. For example, $K = 1$ Pa·s creates two linear fractures directed primarily perpendicular to the less applied stress, while $K = 2$ Pa·s creates multiple linear fractures propagated in the radial direction. $K = 1$ Pa·s leads to more viscosity, which leads to wider radial fractures. These findings show that power-law parameters play a crucial role in fracture initiation, its shape and propagation behavior.

Figure 3a shows the velocity profile of fluid during fracture initiation induced by $K = 2$ Pa·s and $K = 5$ Pa·s (both at $n = 0.2$). Medium viscous fluid with $K = 2$ Pa·s has a higher velocity concentration on the fracture tip, and creates fractures whose orientation is dictated by the applied maximum stress. Therefore, the particles moves toward the less load. On the other hand, fluids with higher viscosity ($K = 5$ Pa·s) produce fractures with relatively lower velocity. In this case, the velocity affects the particles uniformly and exceeds the stresses exerted from all directions leading to a radial fracture shape. Viscosity profiles indicate that fluids with lower viscosity infiltrate wider into the domain, see Fig. 3b. A significant viscosity change can be observed outside the fracture, particularly near the fracture tip and domain boundaries. In the case of $K = 5$ Pa·s, the viscosity does not significantly alter outside the fracture limiting the infiltration through the domain.

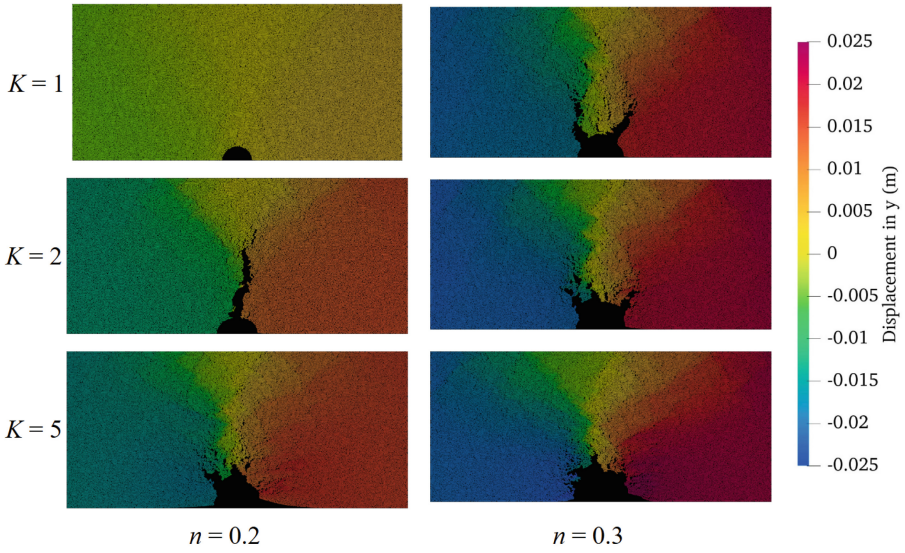

Fig. 2. Fracture initiation of $K = 1$ Pa·s, $K = 2$ Pa·s and $K = 5$ Pa·s at $n = 0.2$ and 0.3.

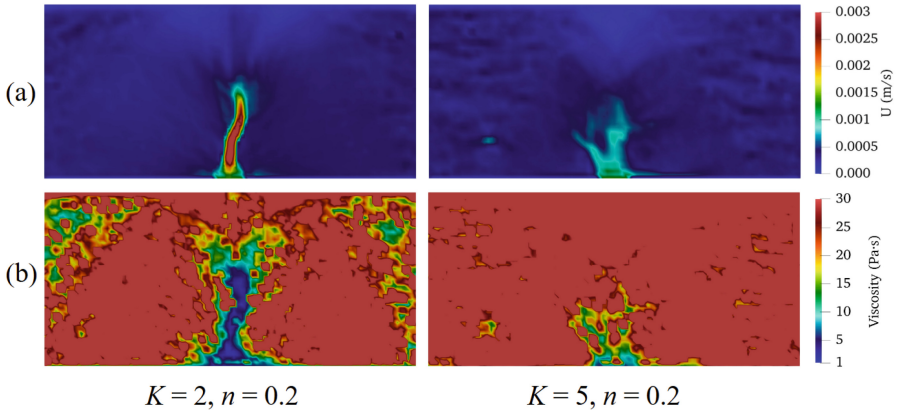

Fig. 3. (a) Velocity and (b) viscosity profile during fracture initiation at $K = 2$ Pa·s and $K = 5$ Pa·s (both $n = 0.2$).

4.2 Injection Pressure During Fracture Initiation

Figure 4a shows the injection pressure over time during fracture initiation at various consistency indices ($K = 1$, 2, 3, 4 and 5 Pa·s) and the same flow behavior index ($n = 0.2$). The behavior of fracture initiation can be evaluated by the evolution of the fluid injection pressure. Initially, the pressure rises and reaches its peak (maximum value of the pressure), indicating the onset of fracturing. Subsequently, the pressure may decrease gradually, drop sharply, or remain stable depending on the rate of fracture

formation. In general, an increase in the consistency index leads to higher injection pressures in all cases observed. Cases of medium and higher consistency indices (K = 2-5 Pa·s) show clear peak pressures, while the lowest consistency index of $K = 1$ Pa·s demonstrates gradual pressure over time with no fracture initiation. Since the flow behavior index is the same in all cases, the pressure evolution over time follows a relatively similar pattern, characterized by a gradual decrease.

Figure 4b demonstrates the pressure injection history at the same consistency index ($K = 2$ Pa·s) and various flow behavior indices ($n = 0.1$, 0.2 and 0.3). Fluid with $n = 0.1$ does not produce any fracture, as indicated by a stable injection pressure throughout the entire simulation. More viscous fluid ($n = 0.3$) results in a higher peak pressure compared to less viscous fluid ($n = 0.2$). Additionally, at n = 0.3, a sharp decrease in injection pressure is observed, indicating a faster fracture opening rate. On the other hand, at $n = 0.2$, the fractures are created in a constant rate, as reflected by a gradual decrease in injection pressure. These findings demonstrate that the flow behavior index magnifies the effect of the consistency index and significantly influences the overall viscosity and fracturing behavior.

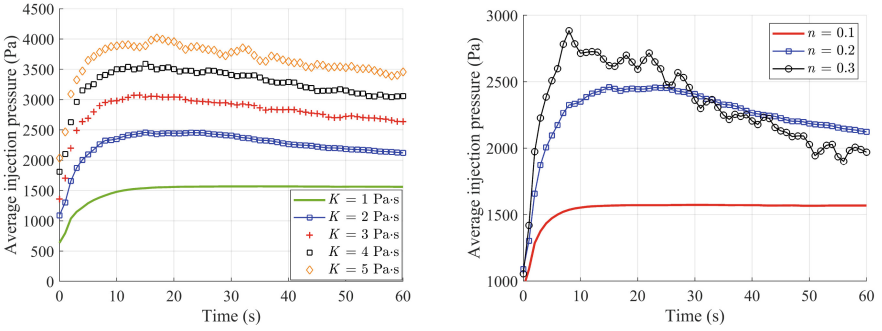

Fig. 4. Comparison of injection pressure over time: (a) $K = 1$, 2, 3 4 and 5 Pa·s (all n = 0.2) and (b) $n = 0.1$, 0.2 and 0.3 (all $K = 2$ Pa·s).

Figure 5 shows the comparison of pressure evolution over time of injected fluids at different CFD time steps of $\Delta t = 10^{-5}$ s (N = 1) and $\Delta t = 10^{-4}$ s (N = 10). From the comparison of injection pressures over time it can be stated that the power law parameters significantly affect the pressure evolution and require careful selection of a time step. For example, the pressure data at $n = 0.1$ and 0.2 is relatively similar in both time step cases. On the other hand, $n = 0.3$ shows significant discrepancies, resulting in an overall RMSRE of 11.56 %. Therefore, at $n = 0.3$ the simulation time step of $\Delta t = 10^{-5}$ s is suitable.

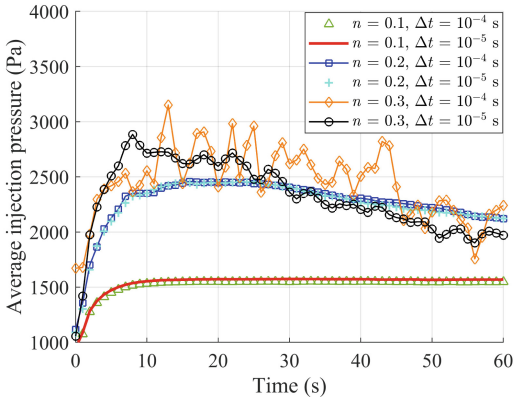

Fig. 5. Injection pressure obtained at CFD time steps of $\Delta t = 10^{-4}$ and $\Delta t = 10^{-5}$ s for cases $K = 2$ Pa·s at $n = 0.1$, 0.2 and 0.3.

Figure 6 represents the Root Mean Squared Relative Error (RMSRE) calculated for various values of the consistency index (K) and the flow behavior index (n). The RMSRE is calculated by comparing simulation results with reference time step of $\Delta t = 10^{-5}$ s against those using increased time step of $\Delta t = 10^{-4}$ s. It is defined as follows:

$$RMSRE = \sqrt{\frac{1}{n}\sum_{i=1}^{n}\left|\frac{p^i_{N=1} - p^i_{N=10}}{p^i_{N=1}}\right|^2} \times 100 \tag{10}$$

where $p^i_{N=1}$ represents the i-th injection pressure computed at $\Delta t = 10^{-5}$ s (N = 1), $p^i_{N=10}$ represents the i-th injection pressure computed at $\Delta t = 10^{-4}$ s (N = 10) and n is the total number of data points. As shown in the figure, the RMSRE is relatively lower for small values of n (0.1 and 0.2) even at higher K. As n increases to 0.3, the errors growth significantly, particularly at the range of $K = 2 - 5$ Pa·s. This shows that the flow behavior index (n) has a more pronounced effect on time step sensitivity compared to the consistency index (K), as evidenced by the larger errors observed in simulations with less shear-thinning fluids ($n = 0.3$).

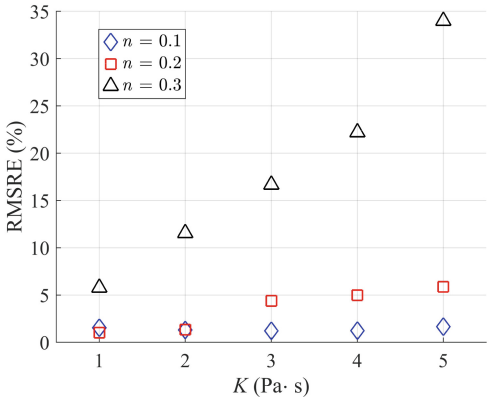

Fig. 6. RMSRE of injection pressure at different power-law parameters.

5 Conclusion

The primary aim of this study is to numerically explore the influence of non-Newtonian rheological parameters on the selection of an appropriate simulation time step size. Particularly, it investigates fracture initiation in weakly cohesive granular media induced by shear-thinning fluids. The flow behavior of non-Newtonian fluids is modeled using the power-law approach, and the drag force acting on particles accounts for their rheological properties. Obtained results show that fracture initiation and propagation behaviors are strongly influenced by power-law parameters. Less viscous fluids tend to create more stress-dependent linear fractures, while more viscous fluids lead to radial fractures with significant grain displacement. Furthermore, in lower-viscosity fluids, the velocity is concentrated at the fracture tip, promoting wider infiltration, while higher-viscosity fluids limit infiltration with a more uniform velocity distribution. An increase in the consistency index at a fixed flow behavior index leads to higher injection pressures during fracture initiation while the overall pressure profile pattern remains similar across all cases. Fluids with a higher flow behavior index result in a higher peak pressure and a more rapid pressure drop, facilitating a faster fracture initiation rate. In contrast, fluids with moderate to lower flow behavior indices lead to lower peak pressures with a more gradual pressure decline, creating fractures at a constant rate. A comparison of injection pressures at different time step sizes shows that the flow behavior index (n) has a stronger influence on CFD time step sensitivity than the consistency index (K). Simulations remain relatively accurate at a higher time step size ($\Delta t = 10^{-4}$ s) for lower flow behavior index values ($n = 0.1$ and 0.2). However, an increasing n to 0.3 results in greater errors, requiring a reduction in the time step size to $\Delta t = 10^{-5}$ s to maintain accuracy. These findings indicate that selecting a suitable time step size is essential for accurately modeling of fracture initiation induced by power-law fluids, particularly for higher flow behavior indices. This study emphasizes the importance of rheological properties in determining fracture propagation patterns, fluid infiltration and simulation

stability, providing valuable insights for modeling non-Newtonian fluid-driven fracture initiation in granular media.

Acknowledgments. The authors acknowledge the support of the research grant no. AP19575428, from the Ministry of Science and Higher Education of the Republic of Kazakhstan. The authors appreciate the support of the Nazarbayev University Faculty Development Competitive Research Grant (NUFDCRG), Grant No. 20122022FD4141.

References

1. Belytschko, T.: An overview of semidiscretization and time integration procedures. Computational Methods for Transient Analysis(A 84-29160 12-64). Amsterdam, North-Holland, 1983, pp. 1–65 (1983)
2. Christopher, R.H., Middleman, S.: Power-law flow through a packed tube. Ind. Eng. Chem. Fundam. **4**(4), 422–426 (1965)
3. Clarke, D.A., Sederman, A.J., Gladden, L.F., Holland, D.J.: Investigation of void fraction schemes for use with CFD-DEM simulations of fluidized beds. Ind. Eng. Chem. Res. **57**(8), 3002–3013 (2018)
4. Courant, R., Friedrichs, K., Lewy, H.: Über die partiellen differenzengleichungen der mathematischen physik. Math. Ann. **100**(1), 32–74 (1928)
5. Duan, K., Kwok, C.Y., Wu, W., Jing, L.: Dem modeling of hydraulic fracturing in permeable rock: influence of viscosity, injection rate and in situ states. Acta Geotech. **13**, 1187–1202 (2018)
6. Goniva, C., Kloss, C., Deen, N.G., Kuipers, J.A., Pirker, S.: Influence of rolling friction on single spout fluidized bed simulation. Particuology **10**(5), 582–591 (2012)
7. Goniva, C., Kloss, C., Hager, A., Pirker, S.: An open source CFD-DEM perspective. In: Proceedings of OpenFOAM Workshop, Göteborg, pp. 22–24 (2010)
8. Hurt, R.S., Germanovich, L.N.: Parameters controlling hydraulic fracturing and fracture tip-dominated leakoff in unconsolidated sands. In: SPE Annual Technical Conference and Exhibition. OnePetro (2012)
9. Issa, R.I.: Solution of the implicitly discretised fluid flow equations by operator-splitting. J. Comput. Phys. **62**(1), 40–65 (1986)
10. Jin, L.: Experimental and numerical modeling of fluid injection into unconsolidated formations (2017)
11. Johnson, K.L., Kendall, K., Roberts, A.: Surface energy and the contact of elastic solids. Proc. R. Soc. Lond. A. Math. Phys. Sci. **324**(1558), 301–313 (1971)
12. Kazidenov, D., Amanbek, Y.: Permeability estimation from pore to darcy in cemented granular media using resolved CFD-DEM model. Results Eng. **24**, 103359 (2024)
13. Kazidenov, D., Amanbek, Y.: CFD-DEM modeling of fracture initiation with polymer injection in granular media. Particuology **97**, 58–68 (2025)
14. Kazidenov, D., Khamitov, F., Amanbek, Y.: Coarse-graining of CFD-DEM for simulation of sand production in the modified cohesive contact model. Gas Sci. Eng. 204976 (2023)
15. Kazidenov, D., Omirbekov, S., Amanbek, Y.: Optimal time-step for coupled CFD-DEM model in sand production. In: Computational Science and Its Applications–ICCSA 2023 Workshops: Athens, Greece, July 3–6, 2023, Preprint. Springer (2023)
16. Kazidenov, D., Omirbekov, S., Zhanabayeva, M., Amanbek, Y.: Experimental and numerical study of the effect of polymer flooding on sand production in poorly consolidated porous media. Geoenergy Sci. Eng. **249**, 213746 (2025)

17. Kissinger, A., et al.: Hydraulic fracturing in unconventional gas reservoirs: risks in the geological system, part 2: modelling the transport of fracturing fluids, brine and methane. Environ. Earth Sci. **70**, 3855–3873 (2013)
18. Kloss, C., Goniva, C., Hager, A., Amberger, S., Pirker, S.: Models, algorithms and validation for opensource dem and CFD-DEM. Progress Comput. Fluid Dyn. Int. J. **12**(2–3), 140–152 (2012)
19. Li, Y., Xu, Y., Thornton, C.: A comparison of discrete element simulations and experiments for sandpiles composed of spherical particles. Powder Technol. **160**(3), 219–228 (2005)
20. Li, Z., Espinoza, D.N., Balhoff, M.T.: Fluid-driven fracture mechanisms in granular media: insights from grain-scale numerical modeling. Granular Matter **23**(4), 1–18 (2021). https://doi.org/10.1007/s10035-021-01161-y
21. Li, Z., Espinoza, D.N., Balhoff, M.T.: Simulation of polymer injection in granular media: implications of fluid-driven fractures, water quality, and undissolved polymers on polymer injectivity. SPE J. **28**(01), 289–300 (2023)
22. Li, Z., Sun, Z., Espinoza, D.N., Balhoff, M.T.: Grain-scale modeling of polymer-driven fracture initiation and wellbore injectivity. In: SPE Improved Oil Recovery Conference, p. D021S034R001. SPE (2020)
23. Shovkun, I., Espinoza, D.N.: Propagation of toughness-dominated fluid-driven fractures in reactive porous media. Int. J. Rock Mech. Min. Sci. **118**, 42–51 (2019)
24. Sun, Z., Balhoff, M.T., Espinoza, D.N.: Fluid injection induced fracture initiation based on a resolved CFD-DEM approach. In: 52nd US Rock Mechanics/Geomechanics Symposium. OnePetro (2018)
25. Sun, Z., Li, Z., Espinoza, D.N., Balhoff, M.T.: Fluid-driven fractures in granular media: insights from numerical investigations. Phys. Rev. E **101**(4), 042903 (2020)
26. Tomac, I., Gutierrez, M.: Coupled hydro-thermo-mechanical modeling of hydraulic fracturing in quasi-brittle rocks using BPM-DEM. J. Rock Mech. Geotech. Eng. **9**(1), 92–104 (2017)
27. Weller, H.G., Tabor, G., Jasak, H., Fureby, C.: A tensorial approach to computational continuum mechanics using object-oriented techniques. Comput. Phys. **12**(6), 620–631 (1998)
28. Zhu, H., Zhou, Z., Yang, R., Yu, A.: Discrete particle simulation of particulate systems: theoretical developments. Chem. Eng. Sci. **62**(13), 3378–3396 (2007)